Research Article | Vol. 32, No. 14 / 1 Jul 2024 / Optics Express 24744

Optics EXPRESS

Window size dependence of gain and bandwidth in avalanche photodiodes with multiple multiplication layers under near Geiger-mode operation

YAN-CHIEH CHANG,[1] YE-KUN WU,[1] CHIA-CHIEN WEI,[2] YOU-CHIA CHANG,[3] TZYY-SHENG HORNG,[4] AND JIN-WEI SHI[1,*]

[1] *Department of Electrical Engineering, National Central University, Jhongli, 320, Taiwan*
[2] *Department of Photonics, National Sun Yat-Sen University, Kaohsiung, Taiwan*
[3] *Department of Photonics, National Yang-Ming Chiao-Tung University, Hsinchu 300, Taiwan*
[4] *Department of Electrical Engineering, National Sun Yat-Sen University, Kaohsiung, Taiwan*
[*] *jwshi@ee.ncu.edu.tw*

Abstract: We consider avalanche photodiodes (APDs) functioning under near Geiger-mode operation for extremely weak light (single or several photons) detection, such as in LiDAR receivers. To meet such demands, APDs which simultaneously have a large active window size, moderate bandwidth (~GHz), and high internal gain (responsivity), are highly desired. However, it is difficult to design APDs capable of meeting the afore-mentioned performance requirements due to the intrinsic limitations of the gain-bandwidth product (GBP). In this work, we demonstrate that the GBP bottleneck in the APDs can be overcome by using multiple (3) $In_{0.52}Al_{0.48}As$ based multiplication (M-) layers with a thick $In_{0.53}Ga_{0.47}As$ absorber (2 µm). Moreover, the characteristic invariant 3-dB bandwidth in our APDs, from low to an extremely high operation gain, becomes more pronounced with an increase of its active window diameter (40 to 200 µm). This characteristic makes it very attractive for collecting weak light in free space as is required for LIDAR receiver applications. Comparison shows that the 200 µm APD exhibits a higher 0.9 V_{br} responsivity (15 vs. 7 A/W), larger maximum gain (460 vs. 110), and higher GBP (468 vs. 131 GHz) than does the 40 µm reference sample and can sustain a constant 3-dB bandwidth (1.4 GHz) over a wide range of operation gains (10 to 460). The dependence of the APD performance on the window size can be attributed to the influence of the surface states on the edge of the etched mesa. Here, we further demonstrate a backside-illuminated structure with a flip-chip bonding package which minimizes this phenomenon in small APDs ensuring high-speed performance. Compared with the top-illuminated reference samples, the flip-chip bonding packaged device shows a further enhancement of the responsivity (10.7 vs. 7 A/W), 3-dB bandwidth (4.1 vs. 3.9 GHz), and saturation current (4.25 vs. 3.6 mA). The excellent static and dynamic performance of our flip-chip APD in turn leads to an unprecedented high velocity sensitivity (5 µm/sec) and superior quality 4-D FMCW LiDAR images compared to that obtainable with p-i-n-based or top-illuminated reference devices with the same small active window size (40 µm).

© 2024 Optica Publishing Group under the terms of the Optica Open Access Publishing Agreement

1. Introduction

Recently, avalanche photodiodes (APDs) capable of operating at around Geiger-mode have been attracting a lot of attention for the detection of extremely weak light (single or a small number of photons) in a variety of applications, such as in single-photon detectors [1,2], time-of-flight (ToF) or FMCW LiDARs [3,4], and optical time domain reflectometers (OTDR) [5]. To satisfy the requirements of such applications, APDs with high-linearity and a wide dynamic range [6,7], which can cover a range from single-photon detection to high saturation output photocurrents [8],

#519504 https://doi.org/10.1364/OE.519504
Journal © 2024 Received 19 Jan 2024; revised 17 Apr 2024; accepted 14 May 2024; published 24 Jun 2024

Optics EXPRESS

with a moderate bandwidth, high-gain (responsivity), and large gain-bandwidth product (GBP) performance are highly desired. Take FMCW LiDAR photo-receivers with APDs inside for example, APDs with a high operation gain, large active window size, and high saturation current can be beneficial for capturing weak reflected light in free space, which can then be amplified through a strong optical local-oscillator (LO) pumping power [4]. Additionally, although less attention is usually paid to the speed performance of the FMCW LiDAR receiver, a wider bandwidth can ensure a larger variation in the beat note frequency centered at the intermediate frequency (IF) in the LiDAR system. This can provide a larger depth of field at the targeted ranging distance. However, due to the additional carrier multiplication process inside the active layer of the APD, the internal carrier response time is usually much longer than that of p-i-n PDs with the same depletion layer thickness. This in turn leads to a greater trade-off between the active window size, responsivity, saturation current, and net optical-to-electrical (O-E) bandwidth when designing the APD [9]. In this work, we investigate, in detail, $In_{0.52}Al_{0.48}As$-based APDs with multiple M-layers and different active window diameters [4,8,10,11] under near Geiger mode operation. The studied structure with it unique M-layer design has already been demonstrated excellent single photon detection efficiency (SPDE), short hold-off time, and good jitter performance under Geiger mode operation [12]. Here, it is further found that the limitations of the GBP in this device can be relaxed, even with an active window diameter as large as 200 µm. A nearly constant 3-dB bandwidth (~1.4 GHz) can be sustained over a wide range of operation gains (around 10 to 460) while preserving a high responsivity (1.55 A/W) at the punch through voltage (V_{pt}). These characteristics are crucial in LiDAR applications for enhancing the sensitivity for weak light detection and minimizing the optical coupling loss from free space to the receiver side. However, these advantages become less apparent when the device window size is downscaled for a larger O-E bandwidth. This problem can be attributed to the influence of the surface states on the edge of the etched mesa. To minimize the problem, the APD is further processed with backside-illuminated structures and a flip-chip bonding package. Compared with the top-illuminated reference sample with the same active window diameter of 40 µm, the flip-chip bonding packaged sample demonstrates a further enhancement of the responsivity (10.7 vs. 7 A/W), with a better 3-dB bandwidth (4.1 vs. 3.9 GHz), and improved saturation current (4.25 vs. 3.6 mA). The excellent static and dynamic performance of the flip-chip APD in turn leads to an unprecedented high velocity sensitivity (5 µm/sec) and superior quality for 4-D FMCW LiDAR [13] imaging compared to that of the p-i-n-based or top-illuminated photoreceivers used for reference.

2. Design and fabrication of the device structure

In this work, APDs with two different triple M-layer designs (devices A and B) are investigated. Conceptual cross-sectional views of the two device structures are shown in Figs. 1(a) and (b), respectively; please note that, for clarity, the device is not drawn to scale. The top view of the fabricated device with an active window (mesa) diameter of 200 (240) µm is shown in the inset to Fig. 1. The exact thickness of each layer is also specified here. The topmost layer is a p + - $In_{0.53}Ga_{0.47}As$ contact layer, followed by a p + -InP window layer, a thick (~2 µm) $In_{0.53}Ga_{0.47}As$ absorber, one composite p-type $In_{0.52}Al_{0.48}As$/InP charge layer, two p-type $In_{0.52}Al_{0.48}As$ charge layers, three intrinsic $In_{0.52}Al_{0.48}As$ multiplication layers and N + $In_{0.52}Al_{0.48}As$ /InP contact layers. Two $In_{0.52}Al_xGa_{0.48-x}As$ graded bandgap layers (GBLs) are introduced at the interfaces between the absorber/window and absorber/multiplication layers. These layers were grown on a semi-insulating (S.I.) InP substrate. Compared with the traditional APD with a single M-layer inside, the M-regions in A and B have been subdivided into different parts by additional charge control layers [4,8,10,11], which results in a stepped electric field profile in the M-region. As shown in Fig. 2(a), the 440 nm thick multiplication (M-) layer in device A is subdivided into three parts, 100, 100, and 240 nm in thickness. This design results in a stepped electric field

Optics EXPRESS

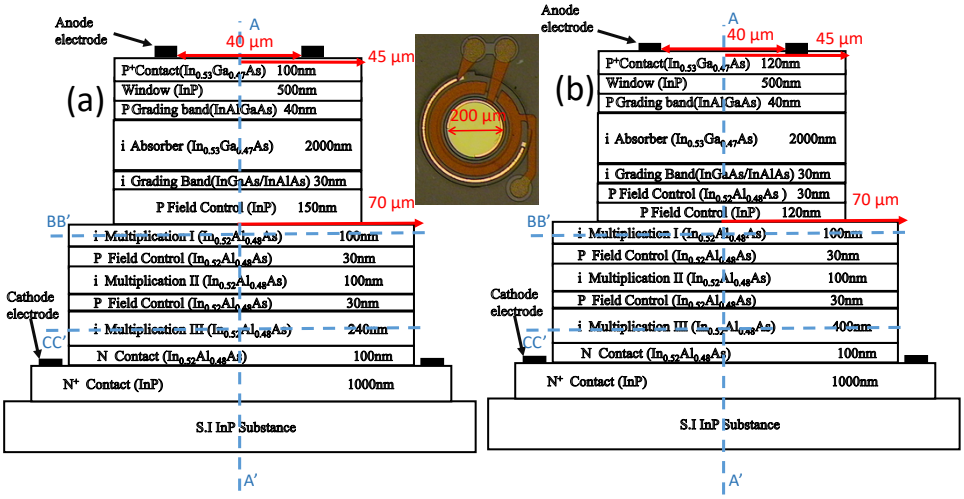

Fig. 1. Cross-sectional view of the demonstrated triple M-layer APD with different thicknesses of the 3rd M-layer: (a) 240 nm (Device A); and (b) 400 nm (Device B). The inset shows a photo of the top-view of the device with an active window diameter of 200 µm. The thickness of each layer is specified in the figures.

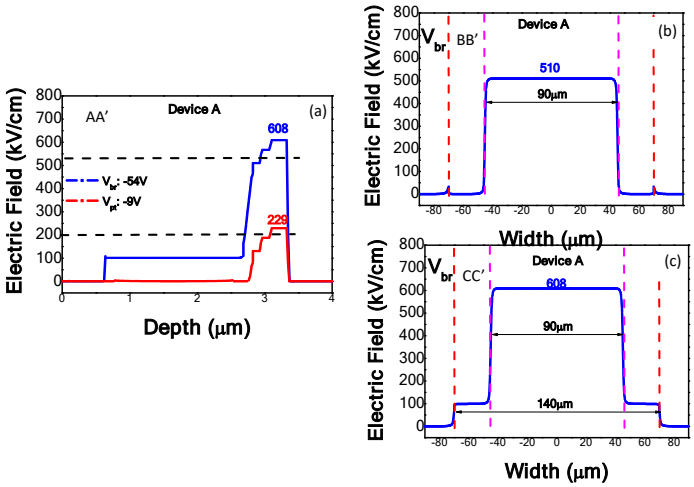

Fig. 2. Electric field profiles at V_{pt} and V_{br} or only V_{br} for device A along the directions: (a) AA'; (b) BB'; and (c) CC'.

profile, with the majority of the avalanche process confined to the 240 nm 3rd M-layer, which has the highest E-field across the entire epi-structure. This leads to a short avalanche delay time, high GBP, and low excess noise. Compared to the direct scaling down of a single M-layer to the same thickness as our 3rd M-layer in the traditional APDs, the inclusion of the 1st and 2nd M-layers in our design can effectively suppress the tunneling leakage process resulting in a lower overall dark current. The main difference between devices A and B is that the 3rd M-layer is thinner in device A than in device B (240 vs. 400 nm). The electric field distribution within the device is simulated using the Silvaco Technology Computer Aided Design (TCAD) [14] tools. Since both devices (A and B) share the same etched mesa structure and very similar epi-layer designs,

Optics EXPRESS

their E-field distributions are almost the same. Figure 2 shows the electric fields for device A at the V_{pt} and breakdown (V_{br}) voltage along the vertical (AA') and horizontal (BB' and CC′) directions (through the 1st and 3rd M-layers, respectively), as shown in Fig. 1. The influences of E-field distributions on the dynamic and static performances of demonstrated APDs will be discussed in greater detail later.

3. Measurement results

The values of V_{br} and V_{pt} were measured and specified in the I-V curves for devices A and B, as shown in Figs. 3 and 4, respectively. In this study, devices A and B were fabricated with three different sizes of active window (with diameters of 200, 60, and 40 µm) and differences in performance investigated. All the results shown in this work are obtained with the wavelength of the incident light fixed at 1.55 µm. The V_{pt} responsivity (~1.5 A/W) of the 200 µm window size (WS) design corresponds to an external quantum efficiency of 124%, which indicates that the avalanche gain happens under the V_{pt} bias. This phenomenon can be attributed to the charge layer doping being high enough to confine the external applied electric field inside the M-layers, to let it be higher than the critical field when the bias voltage reaches V_{pt}. This characteristic is very commonly reported in APDs [4,10,11]. Here, the theoretical maximum responsivity for the unit gain, calculated based on the thickness of the absorption layer (~2 µm) and assuming a zero optical coupling loss, is 1 A/W. As can be seen, when the active window diameters of devices A and B are the same, the responsivity values are close, at 0.9 (0.95) V_{br}. With the largest active window diameter of 200 µm, the measured responsivity of device A can be as high as 15 A/W under 0.9 V_{br} operation. Furthermore, for both devices, the measured responsivity gradually increases as the size of the active window increases. Device A with an active diameter of 200 µm exhibits a higher 0.9 V_{br} responsivity (15 vs. 7 A/W) and a larger maximum gain (460 vs. 110) than is the case for the 40 µm reference device This phenomenon is reproducible and repeatable for both APD designs (A and B). The optical coupling loss should be nearly zero due to the fact that the spot size of the optical signal launched through the lens fiber is much smaller (~10 vs. 40 µm) than that of the minimum window size.

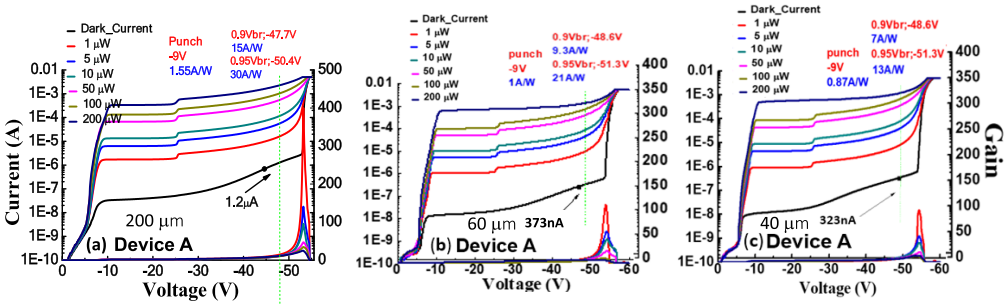

Fig. 3. Bias dependent dark current, photocurrent, and operation gain measured under different optical pumping powers for Device A with active window diameters of: (a) 200 µm; (b) 60 µm; and (c) 40 µm.

The dependence of the APD performance on the window size might be attributable to the influence of surface states on the edge of the etched mesa and the phenomenon of carrier transport in the transverse direction of the mesa. As can be clearly seen in Figs. 2(b) and (c), with our composite charge layer design [15] we can exactly zero the E-field in the sidewall of the 1st M layer. However, in the bottommost 3rd M-layer with the E-field region, the E-field at the sidewall is around 100 kV/cm. This transverse E-field accelerates the lateral diffusion of carriers generated by the multiplication process and enhance the surface recombination process in the sidewall of

Optics EXPRESS

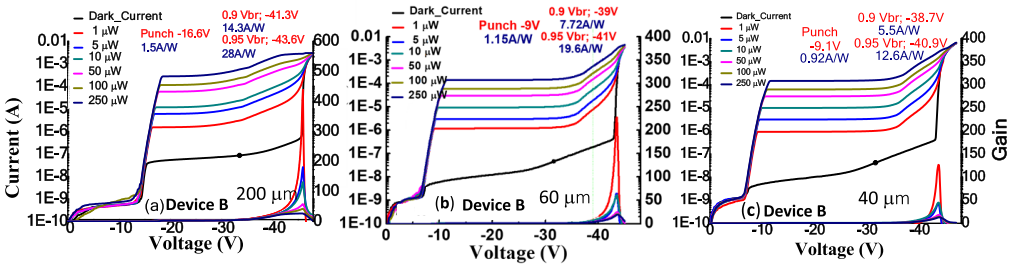

Fig. 4. Bias dependent dark current, photocurrent, and operation gain measured under different optical pumping powers for Device B with active window diameters of: (a) 200 μm (b) 60 μm; and (c) 40 μm.

the 3rd M-layer. In the case of large window size (WS) devices (~200 μm), we can expect the surface recombination to be much less pronounced than that occurring in the smaller window devices because of the large difference in the transverse carrier drift distance (145 vs. 70 μm, as shown in Fig. 1) from the center to the sidewall of the 3rd M-layer. This layer has the highest E-field and most significant avalanche process among these three M-layers. Such a long lateral drift distance (145 μm) in the large WS device leads to most of the carriers being collected by the bottommost n^+ contact layer before being captured in the surface states of the etched sidewall. Furthermore, the difference in responsivity between large and small WS APDs becomes more significant under low excitation power (1 μW) and extremely high gain (>100) operation (near Geiger-mode). This is because a higher avalanche gain is always accompanied by a slower carrier multiplication process in the vertical direction, which would then enhance the probability of lateral carrier recombination in the surface state of the etched sidewall. The advantage of a large WS APD, which can effectively suppress this sort of carrier lateral transport, i.e., 2-D effect, thus becomes more apparent.

The dark current measurements of our devices with three different WSs also lend support to the assumption that the surface state plays a more important role in the static performance of small device. There are two major contributors of dark current in APD device. One is surface leakage, the other is leakage of the bulk current, which are proportional to the surface area and volume of the active device, respectively. The dark currents corresponding to device A with the three different window sizes (WS: 40, 60, 200 μm), under the same bias voltage, are 0.9 V_{br} is 0.32, 0.37, and 1.2 μA, respectively, as specified on Fig. 3. As can be seen in Fig. 1, each WS is comprised of two different active mesa diameters. For example, for 40 and 60 μm WS devices the up (down) active mesa diameters are 90 (110) and 140 (160) μm, respectively. The corresponding surface area ratio is around 1.2, which is very close to the measured dark current ratios (0.32 and 0.37 μA). However, for WSs of 200 and 40 μm, there is a 6 and 2.5 times difference in their volumes and surface areas, respectively. From the ratio of the measured dark current (~4) between these two devices, we can conclude that surface leakage current plays a less vital role in the total measured dark current of the large device.

Figures 5 and 6 show the measured optical-to-electrical (O-E) frequency responses of devices A and B with two different WSs (200 and 40 μm), respectively. As can be seen, in most of the measured traces, there is a minor peaking effect (0.5 to 1 dB) at around 0.5 GHz. This phenomenon is more pronounced for the top-illuminated APDs, which can be attributed to the natural resonance frequency of the probe pad layout. On the other hand, this small resonance is less apparent in the flip-chip bonding sample, as illustrated in Fig. 11, since the pad layout has been modified.

Optics EXPRESS

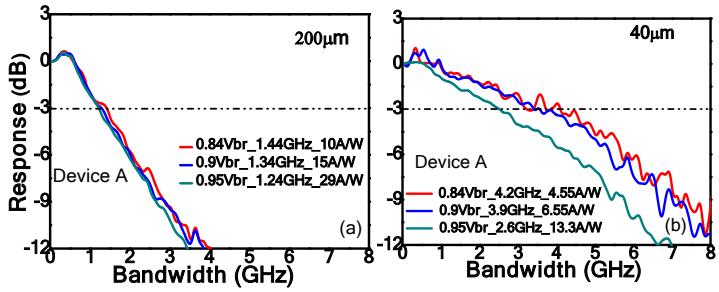

Fig. 5. Measured bias dependent O-E frequency responses under an optical pumping power of 1 μW of device A with active window diameters of: (a) 200 μm and (b) 40 μm.

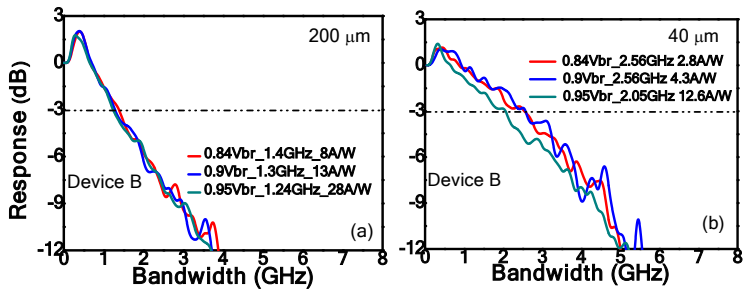

Fig. 6. Measured bias dependent O-E frequency responses under an optical pumping power of 1 μW of device B with active window diameters of: (a) 200 μm and (b) 40 μm.

We can clearly see that thinning the 3rd M-layer causes device A to exhibit a much faster speed performance than that of device B, even for cases with the same WS of 40 μm and bias voltage of 0.9 V_{br}. This indicates that most of the avalanche processes occur in the 3rd M-layer and that avalanche delay is the dominant bandwidth limiting factor in both devices. However, when the WS increases to 200 μm, both devices exhibit the same 3-dB bandwidth at around 1.4 GHz. Furthermore, such speed performance from moderate to very high responsivity (gain) is invariant. This phenomenon contrasts with that reported for most APDs, which usually exhibit a monotonic decrease of bandwidth with an increase of the operation gain [9,16]. The similar bandwidth performance of devices A and B is attributed to the switching in the dominant bandwidth limiting factor from the avalanche delay time to the RC time constant in the case of a large WS. The equivalent circuit modeling technique was adopted to determine whether it was the transit or the RC-delay time which was the dominant bandwidth limiting factor for the APDs with different WSs. This was done by extracting the transit and RC-limited bandwidths of both device structures (A and B) with different WSs (40, 60, and 200 μm), under 0.9 V_{br} operation [11]. For further details about our APD modeling processes the interested reader can refer to our previous work [11].

Figure 7 shows the RC, transit time, and measured/fitted O-E frequency responses of device A extracted under 0.9 V_{br}. As can be seen in Fig. 7(c), with a WS of 200 μm, the net 3-dB O-E bandwidth (1.4 GHz) is limited by the RC value (1.9 GHz) rather than the transit time limited bandwidth (~4.5 GHz). From the extracted RC-limited bandwidth (f_{RC}) and the measured net O-E bandwidth (f_3 dB) for each device size, we can also obtain the transit time limited bandwidth (f_t) for devices A and B [11] as follows:

$$\frac{1}{f_{3dB}^2} = \frac{1}{f_{RC}^2} + \frac{1}{f_t^2} = (2\pi RC)^2 + \frac{1}{f_t^2}. \tag{1}$$

Optics EXPRESS

where R is the sum of the parasitic resistance and the load resistance (50 Ω) and C is the total capacitance. Figure 8 depicts the values of $(1/f_{RC})^2$ versus $(10/f_{3dB}^2)$ of devices A and B with 3 different sized WSs. The internal f_t in our devices can be obtained from the intercepts along the y-axis as shown in Fig. 8 [11]. The f_t values obtained are approximately 4.4 and 2.6 GHz for devices A and B, respectively, which closely match the transit time limited bandwidth obtained using the equivalent circuit modeling technique, as illustrated in Fig. 7. Moreover, device A, with its thinner 3rd M-layer, exhibits a larger f_t than does device B, due to its shorter avalanche delay time, which leads to a higher net O-E bandwidth (4 vs. 2.6 GHz), as shown in Figs. 5 and 6.

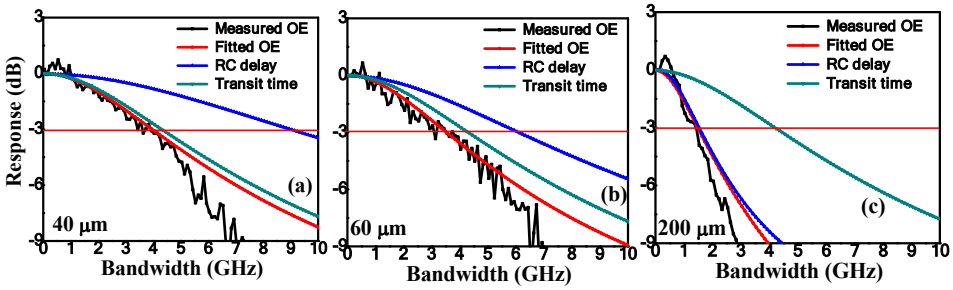

Fig. 7. Measured O-E, extracted RC-limited, transit time, and fitted O-E frequency responses for device A with different active window diameters of: (a) 40 µm; (b) 60 µm; and (c) 200 µm

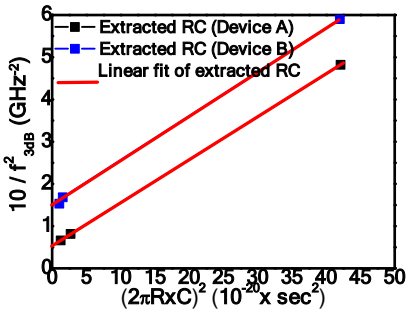

Fig. 8. Extracted $(1/f_{RC})^2$ versus measured $(10/f_{3dB}^2)$ for devices A and B with 3 different WSs.

Figures 9(a) and (b) show a comparison of the GBP performances obtained with both device designs, with large (200 µm) and small (40 µm) WSs. Figure 9(c) shows all the extracted GBP values for both these devices with three different WSs. Obviously, in both devices, with a large WS (200 µm), the demonstrated triple M-layer design can overcome the fundamental limitations of the GBP encountered in the traditional APD and eliminate degradation in the O-E bandwidth under extremely high gain operation (> 400). However, the advantages of this triple M-layer design are less apparent for small WS (40 and 60 µm) devices.

The superior GBP performance obtained with our design compared to that of the traditional APD with a single M-layer is because each M-layer in our triple M-layer design can contribute to the overall multiplication gain and it is thus not necessary to push each M-layer into deep avalanche mode for the desired high-gain operation. For more details about the working principles of our multiple M-layer design please refer to our previous work [10,11]. However, just like what has been reported for most high-speed APDs [9,16], with small WSs, there is a monotonic degradation in the measured bandwidths of both devices (A and B) under high gain operation (>10). Moreover, the GBP values are much smaller than those corresponding to large WS cases.

Optics EXPRESS

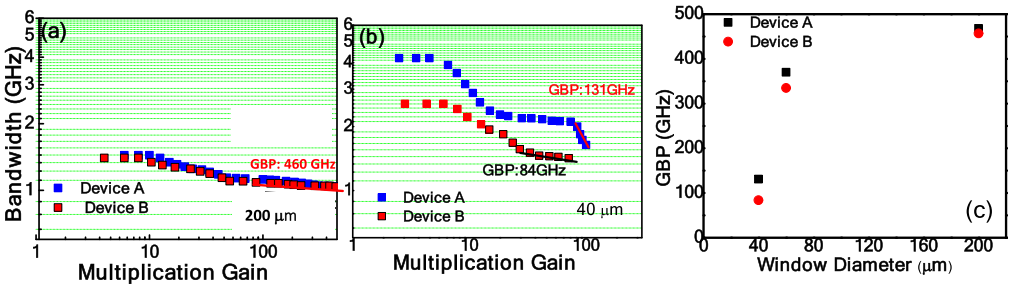

Fig. 9. Measured 3-dB O-E bandwidths versus multiplication gain of devices A and B at a low (1 μW) optical pumping power for different active diameters of: (a) 200 μm and (b) 40 μm. (c) The extracted GBP values of devices A and B with different window diameters.

As can be clearly seen in Fig. 9(b), under high gain operation (~100), the O-E bandwidth degrades to only 1.3 GHz. Based on the extracted f_t value (~4.4 GHz) of device A under 0.9 V_{br} operation, as noted in Fig. 7, we can conclude that there is a significant decrease in f_t (4.4 to 1.3 GHz) when the operation gains increase from 10 to 100 for small WS (40 μm) devices. Nevertheless, for a size of 200 μm, the net f_3 dB bandwidth is nearly invariant which reflects the truth that the decrease of f_t is not so significant in the large WS APD under extremely high gain (> 100) operation. Such distinct differences in internal response time and GBPs between APDs with large and small WSs can be attributed to the more pronounced influence of surface states at the edge of the 3rd multiplication layer in small WS APDs under extremely high gain operation (>100), as illustrated in Figs. 3 and 4. This in turn leads to a degradation of responsivity, smaller maximum gain (110 vs. 460), and a much worse GBP performance in the small WS APDs. Table 1 shows the high-performance benchmark for APDs for LiDAR applications. As can be seen in Table 1, our multiple M-layer APD with the 200 μm WS outperforms the APDs obtained from different suppliers [17–19] with respect to gain, responsivity, and smaller V_{br}, while maintaining a better O-E bandwidth. Although our demonstrated APD exhibits the highest dark current among these devices, the 1 μA leakage current of our device should still be acceptable for most practical applications [20]. This is because the RMS noise current of the next generation of low-noise amplifiers (LNAs) or trans-impedance amplifiers (TIAs), which are integrated with APDs, is usually much larger than 1 μA [20]. In this scenario, the sensitivity of the receiver is limited by excess noise in the APD rather than the dark current and the thin effective M-layer in our multiple M-layer design should be capable of providing high-speed and low excess noise performance [7]: see Table 1. The exact values of the excess noise of the APDs demonstrated in this study, will be studied in future work.

Flip-chip bonding packaging was used to further improve the GBP performance of the small WS device A for high-speed performance. Figure 10 shows a top-view of the device before and after flip-chip bonding packaging. Backside illuminated structures have several advantages over top-illuminated structures. First, the fully covered topmost p-contact metal can eliminate the photocurrent crowding effect at the edge of the ring contact that occurs in the top-illuminated structure. This characteristic can provide a higher saturation current [21] and can minimize the influence of the etched sidewall on the multiplication gain, as demonstrated in Figs. 3 and 4. Secondly, the fully covered p-metal surface serves as a reflector, which can fold the optical absorption path and further enhance the responsivity of the APD. Finally, for the same WS, the backside structure can be realized using a smaller active mesa diameter than is the case for a top-illuminated structure because of the elimination of the ring contact metal structure. The smaller active mesa size leads to a smaller junction capacitance, a larger RC-limited bandwidth, and usually a wider net O-E bandwidth. By combining the optimized flip-chip bonding package

Optics EXPRESS

Table 1. Benchmark APD performance in LiDAR applications

Parameters	Condition	Excelitas (C30662)	Hamamatsu (G14858-0020AB)	GaAsSb/ AlGaAsSb	Our topside APD	Unit
Active diameter	-	0.2	0.2	0.2	0.2	mm
Gain	Maxima	20 (useable)	30	278	440 20 (useable)	-
Responsivity	M = 1	0.93	0.8	0.17	1.5	A/W
Bandwidth	M = 10	0.85	0.9	0.7 at M = 25	Around 1.3 at M = 10 to 400	GHz
Breakdown voltage	V_{br}	50	65	70	53	V
Dark current	$0.95V_{br}$	45	20	480	1000	nA
Ref no.	-	13	14	15	This work	-

with a backside illuminated PD structure, a further enhancement of bandwidth and responsivity as compared to those of the top-illuminated reference structure has been demonstrated [22].

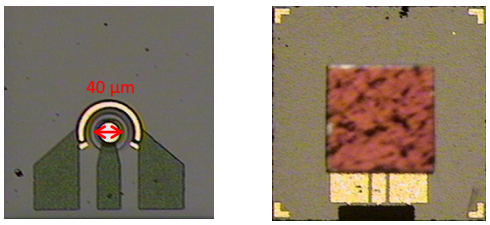

Fig. 10. Top-views of the demonstrated APDs before and after flip-chip bonding.

Figures 11(a) to (c) show the measured I-V curves, O-E frequency responses, and bandwidth versus gain of device A after flip-chip bonding packaging. The active window (mesa) is 40 (50) µm in diameter. We can clearly see that compared with the performance of the top-illuminated reference structure with the same WS, it exhibits a much higher 0.95 V_{br} responsivity (17.2 vs. 13 A/W), a wider 3-dB O-E bandwidth (4.8 vs. 4 GHz), and a larger GBP (150 vs. 131 GHz). As discussed in the introduction, the high saturation current output performance of the APD is important for FMCW LiDAR applications. Figures 12(a) and (b) show the measured DC photocurrent versus optical pumping power of the flip-chip bonded structure and the top-illuminated reference sample measured under different reverse bias voltages. As expected, the saturation current of the flip-chip bonded structure is higher (4.25 vs. 3.6 mA) than that of the reference sample.

The superior performance results obtained for our backside-illuminated APD compared to the commercially available p-i-n PD photoreceivers and top-illuminated reference samples for LiDAR application were verified by using them in a 4-D FMCW LiDAR system. For details about our LiDAR setup please refer to our previous work [13]. The IF frequency chosen for our system was 2.4 GHz, which leads the required bandwidth on the receiver side to be around the same frequency range (~3 GHz). Figure 13 shows examples of 3-D location and velocity images captured at an extremely low speed of movement of 10 µm/sec. Images were captured using a commercially available p-i-n PD photoreceiver (Thorlabs, RXM42AF) and our backside-illuminated APD with a WS of 40 µm, as described above. The inset to Fig. 13 shows a photo of our system setup. The system simultaneously sensed the distance and the velocity of the I, ♡, and U-shaped targets,

Optics EXPRESS

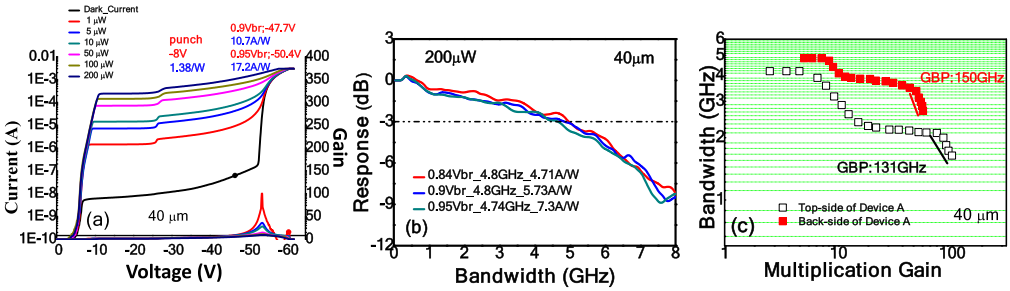

Fig. 11. (a) Measured bias dependent dark current, photocurrent, and operation gain under different optical pumping powers for device A (WS: 40 μm) after flip-chip bonding packaging: (b) measured bias dependent O-E frequency response of the same device; (c) measured 3-dB O-E bandwidths versus multiplication gain for device A with top- and backside illuminated structures.

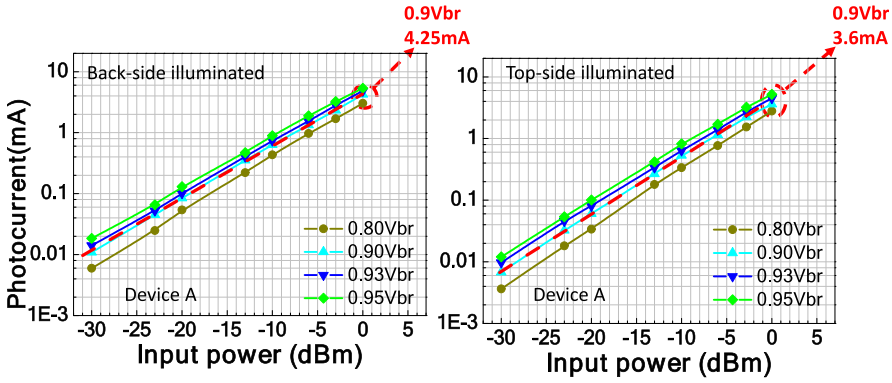

Fig. 12. Measured DC output photocurrent versus input optical input power for device A with a: (a) backside-illuminated and (b) topside illuminated structure.

which were made from Styrofoam wrapped in retroreflective tape. The ♡-shaped object was placed on a motorized linear stage which could be moved at a given speed, while the I and U-shaped targets remained static. The relative distances to the I, ♡, and U-shaped targets were 2, 7, and 12 cm, respectively. Note that the azimuth and elevation for 4D measurement were obtained by 40 by 40 pixel scanning in this work. As can be seen in Fig. 13, a clear 3-D image of the location can be constructed based on the images from both types of photoreceivers, but a much better quality velocity image can be obtained with the APD device than that obtainable using the p-i-n PD device, due to the higher signal-to-noise (S/N) ratio for each pixel [13]. Figure 14 shows a comparison between the LiDAR images based on the top and backside-illuminated APDs. Here, both devices share the same WS of 40 μm. Obviously, the velocity sensitivity can be further enhanced to as low as 5 μm/sec through the use of the backside-illuminated APD on the receiver side. This enhancement is possible because of the superior gain and responsivity performance compared to that of the top-illuminated reference model.

Optics EXPRESS

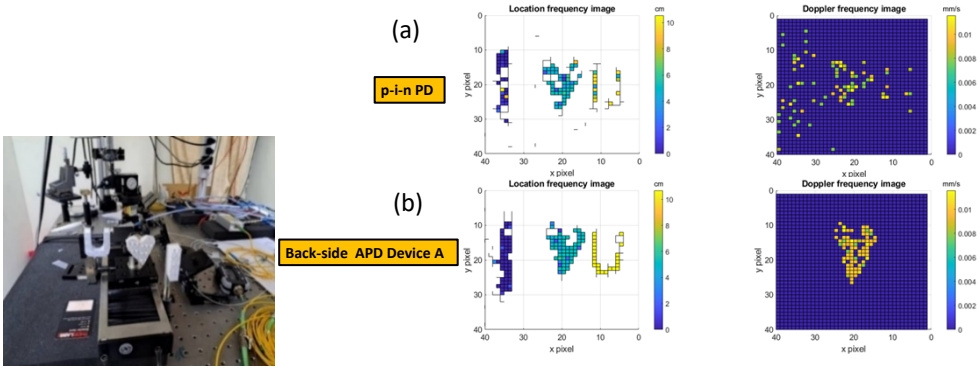

Fig. 13. Measured 4-D images of motion at 10 µm/sec with the: (a) p-i-n PD; and (b) device A in the receiver-end of FMCW LiDAR setup. The inset shows the placement of the targets (I, ♡, and U) at a specified distance for testing.

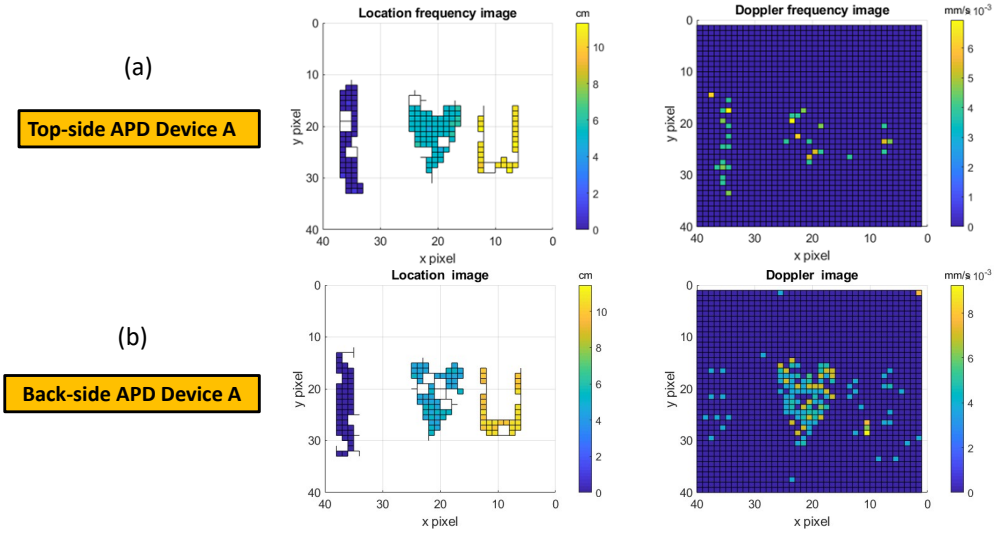

Fig. 14. Measured 4-D images of motion at 5 µm/sec with device A for: (a) topside illuminated; and (b) backside illuminated structures in the receiver-end of the FMCW LiDAR setup.

Optics EXPRESS

4. Conclusions

In conclusion, by enlarging the active WS in multiple M-layer APDs to 200 µm, we can minimize the influence of surface recombination on the static and dynamic performance to overcome the limitations of the maximum gain and GBPs encountered in traditional APDs. The characteristics of the demonstrated APD with large WSs make it very suitable for weak light detection, such as required for LiDAR applications. Moreover, in order to suppress the surface recombination in the small WS (40 µm) APD for high-speed performance, we demonstrated backside-illuminated structures with flip-chip bonding packaging. After installing this packaged module in the receiver-end of an established 4-D FMCW LiDAR system, we obtained much better quality 4-D images than those which could be obtained with the top-illuminated reference structure. A state-of-the-art velocity sensitivity of 5 µm/sec was achieved with our LiDAR system with the flip-chip bonding packaged APD inside.

Funding. National Science and Technology Council (112-2622-8-008 -004 -).

Disclosures. The authors declare no conflicts of interest.

Data availability. Data underlying the results presented in this paper are not publicly available at this time but may be obtained from the authors upon reasonable request.

References

1. M. Liu, C. Hu, X. Bai, *et al.*, "High-performance InGaAs-InP single-photon avalanche photodiode," IEEE J. Sel. Top. Quantum Electron. **13**(4), 887–894 (2007).
2. F. Signorelli, F. Telesca, E. Conca, *et al.*, "Low-Noise InGaAs/InP Single-Photon Avalanche Diodes for Fiber-Based and Free-Space Applications," IEEE J. Sel. Top. Quantum Electron. **28**(2), 3801310 (2022).
3. S. Donati, G. Martini, Z. Pei, *et al.*, "Analysis of Timing Errors in Time-of-Flight LiDAR Using APDs and SPADs Receivers," IEEE J. Sel. Top. Quantum Electron. **57**(1), 7500108 (2021).
4. Z. Ahmad, S.-I Kuo, Y.-C. Chang, *et al.*, "Avalanche Photodiodes with Dual Multiplication Layers and Ultra-High Responsivity-Bandwidth Products for FMCW Lidar System Applications," IEEE J. Sel. Top. Quantum Electron. **28**(2), 3800709 (2022).
5. https://www.excelitas.com/file-download/download/public/101431?filename=C30733EH-1_Datasheet.pdf.
6. T. Beckerwerth, R. Behrends, F. Ganzer, *et al.*, "Linearity Characteristics of Avalanche Photodiodes for InP Based PICs," IEEE J. Sel. Top. Quantum Electron. **28**(2), 3803408 (2022).
7. Hao-Yi Naseem Zhao, Andrew H. Jones, Rui-Lin Chao, *et al.*, "High-Speed Avalanche Photodiodes with Wide Dynamic Range Performance," J. Lightwave Technol. **37**(23), 5945–5952 (2019).
8. Yi-Shan Lee and Jin-Wei Shi, "High-performances dual M-layers avalanche photodiodes from single-photon detection to high saturation output current," Proc. SPIE **12089**, 120890F (2022).
9. M. Nada, Y. Yamada, and H. Matsuzaki, "Responsivity-Bandwidth Limit of Avalanche Photodiodes: Toward Future Ethernet Systems," IEEE J. Sel. Top. Quantum Electron. **24**(2), 3800811 (2018).
10. Z. Ahmad, P.-S. Wang, Naseem, *et al.*, "Avalanche photodiodes with multiple multiplication layers for coherent detection," Sci. Rep. **12**(1), 16541 (2022).
11. A. Naseem, P.-S. Wang, Z. Ahmad, *et al.*, "Top-illuminated Avalanche Photodiodes with Cascaded Multiplication Layers for High-Speed and Wide Dynamic Range Performance," J. Lightwave Technol. **40**(24), 7893–7900 (2022).
12. Yi-Shan A. Lee, Yan-Min Liao, Ping-Li Wu, *et al.*, "$In_{0.52}Al_{0.48}As$ Based Single Photon Avalanche Diodes with Stepped E-field in Multiplication Layers and High Efficiency Beyond 60%," IEEE J. Sel. Top. Quantum Electron. **28**(2), 3802107 (2022).
13. Yu-Xiang Lin, Zohauddin Ahmad, Sung-Yi Ou, *et al.*, "A 4-D FMCW LiDAR With Ultra-High Velocity Sensitivity," J. Lightwave Technol. **41**(21), 6664–6674 (2023).
14. Silvaco, 2811 Mission College Boulevard, 6th floor, Santa Clara, CA 95054 (https://silvaco.com/)
15. A. Naseem, Z. Ahmad, Y.-M. Liao, *et al.*, "Avalanche Photodiodes with Composite Charge-Layers for Low Dark Current, High-Speed, and High-Power Performance," IEEE J. Sel. Top. Quantum Electron. **28**(2), 3801910 (2022).
16. G. S. Kinsey, J. C. Campbell, and A. G. Dentai, "Waveguide avalanche photodiode operating at 1.55 µm with a gain-bandwidth product of 320 GHz," IEEE Photonics Technol. Lett. **13**(8), 842–844 (2001).
17. https://www.excelitas.com/product/c30662eh-1-ingaas-apd-200um-18.
18. https://www.hamamatsu.com/content/dam/hamamatsu-photonics/sites/documents/99_SALES_LIBRARY/ssd/g14858-0020aa_kapd1068e.pdf.
19. S. Lee, X. Jin, H. Jung, *et al.*, "High gain, low noise 1550 nm GaAsSb/AlGaAsSb avalanche photodiodes," Optica **10**(2), 147–154 (2023).
20. M. Huang, S. Li, P. Cai, *et al.*, "Germanium on Silicon Avalanche Photodiode," IEEE J. Sel. Top. Quantum Electron. **24**(2), 3800911 (2018).
21. X. Li, N. Li, S. Demiguel, *et al.*, "A comparison of front- and backside-illuminated high-saturation power partially depleted absorber photodetectors," IEEE J. Sel. Top. Quantum Electron. **40**(9), 1321–1325 (2004).
22. A. Naseem, N.-W. Chen, S. H. Parvez, *et al.*, "Simultaneous enhancement of the bandwidth and responsivity in high-speed avalanche photodiodes with an optimized flip-chip bonding package," Opt. Express **31**(16), 26463–26473 (2023).